Tunable Piezoresistivity of Low Percolation Threshold Micro-Nickel Wires/PDMS Conductive Composite Regulated by Magnetic Field

Shaoyu Niu[†], Shan Wang[†], Qilong Yan[†], Zheyi Han[†], Xiang Lou[†], Qiyang Li[⊥],

Zongrong Wang*, Chi Wah Leung *[§], Shaoxing Qu*[⊥]

† State Key Lab of Silicon Materials, School of Materials Science and Engineering, Zhejiang University, Hangzhou, 310027, China

§ Department of Applied Physics, The Hong Kong Polytechnic University, Hung Hom, Hong Kong, China

⊥ State Key Laboratory of Fluid Power & Mechatronic System, Key Laboratory of Soft Machines and Smart Devices of Zhejiang Province, Center for X-Mechanics, and Department of Engineering Mechanics, Zhejiang University, Hangzhou, 310027, China

Corresponding author

E-mail: zrw@zju.edu.cn, squ@zju.edu.cn, apleung@polyu.edu.hk

Abstract

High performance flexible pressure sensors with tunable piezoresistivity are proposed with percolative composites as single sensing layer using micro-nickel (μNi) wires as conductive filler and polydimethylsiloxane (PDMS) as matrix. The μNi wires were dispersed into PDMS and cured in a magnetic field of 17 mT to make the μNi wires aligned along the direction of magnetic field. The ultra-low percolation threshold (0.31vol%) by more than an order of magnitude lower than 4.79 vol% of control sample without magnetic field has been achieved. Furthermore, pressure sensor with microhump microstructures based on Ni@PDMS composites with volume fraction of 0.6 vol% molded by sandpaper exhibits ultrahigh averaged sensitivity (8706 kPa^{-1}), a wide sensing range of 1 kPa to 120 kPa and fast response time of ~22 ms. The sensor was used to monitor different frequencies and flow rates of water flow in a pump-driven system that mimics the pulsatile behavior of coronary artery and judge whether the graft vessel is blocked or not, showing high potential in clinical diagnosis.

Keywords: percolative composite; single sensing layer; piezoresistive sensors; high sensitivity; magnetic field

1. Introduction

Flexible pressure sensors are crucial building blocks for applications in real-time human health monitoring, artificial electronic skin, human-machine interaction, etc [1-5]. Nowadays, coronary heart disease (CHD) and its complications are one of the main diseases that cause high fatality rate in the world [6, 7]. Coronary artery bypass grafting (CABG) remains the standard surgery for patients with three vessels or left main coronary artery disease, which are both serious types of CHD [8, 9]. During the surgery, narrowing or even blocking in the interconnecting part between the graft vessel and coronary is highly possible to occur [10]. Then verifying whether narrowing or blocking occurs or not is a key step to assure the success of the surgery. There are several techniques available for direct intra-operative assessment of graft patency and among these techniques, transit time flow measurement (TTFM) and conventional angiography (CA) are the most widely used ones [11]. TTFM based on transit-time ultrasound technology could provide blood flow data of the graft and display it in waveform [12]. However, the accuracy of TTFM can be easily affected, especially in low flow conditions that is common in surgeries [13]. Thus, TTFM cannot evaluate the patency of grafts sensitively in low flow conditions. CA is another method for evaluating graft state and it can provide visualization of the blood flow within the graft. However, its intra-operative operation highly relies on advanced clinical instruments and suffers from the potential side effect due to the application of nephrotoxic contrast agents [14]. Thereby, it is of importance to develop a method that could obtain signals sensitively and easily under low flow conditions. Actually, the frequency and flow rates of the blood flow will become different from the normal blood vessels when the blood vessel is blocked or narrowed, and then the pressure on the blood vessel will make a difference [15]. Flexible pressure sensors have been proved to transform the change of pressure signal to electrical signal through the deforming of the sensing layer [16]. As a result, the change of signal caused by the narrowing or blocking can also be detected by a pressure sensor if the sensor is in contact with the tube. Therefore, if a high-performance flexible pressure sensor with high sensitivity and fast response time could be developed, it could be used to timely detect the change of blood flow during surgery and provide useful reference for doctors.

Recently, piezoresistive pressure sensors have attracted wide attention for their advantages, including high sensitivity, high resolution and fast response time [17-19]. And in most widely reported devices, the sensing layer is composed of deforming material and conducting material [20, 21]. However, the mechanical properties varied a lot between these two materials to cause detachment or crack problems [22]. To avoid the property mismatch issue, conductive polymer composites (CPCs) have been proposed to replace the two-layer structure as a single sensing layer to enhance the performance of sensors [23]. As a matter of fact, CPCs are usually produced by introducing conductive fillers (such as graphene [24], carbon nanotubes (CNTs) [25], carbon black [26] and metallic nanowires [27])with high electrical conductivity into flexible polymer matrix (such as polydimethylsiloxane (PDMS) [28], polyurethane (PU) [29] and Ecoflex [30]).

According to the percolation theory[31, 32], CPCs could achieve a transition from insulator to conductor when the filler content is high enough to build up the conductive networks and the corresponding volume fraction of filler is called the percolation threshold. However, the matrix will be strengthened and Young's modulus of composites will be higher to make it harder to deform under the same loading [33]. In fact, the percolation threshold is greatly influenced by the distribution and geometric parameters of fillers, such as filler shape and aspect ratio [34]. The percolation threshold decreases with the increase of aspect ratio and better dispersion of fillers. Although some efforts have been made to lower the percolation threshold of composites, there are still several major issues to be concerned: 1) fillers with nanoscopic dimensions are more likely to agglomerate in polymer matrix due to strong inter-van Waals forces; 2) the sensitivity and sensing pressure range are not controllable when conductive fillers are randomly distributed in the matrix; 3) the widely reported metallic wires are mainly noble metal, such as silver and gold. Hence, a low-cost controllable CPCs system with a low percolation threshold needs to be developed, especially based on conductive fillers with a large aspect ratio and a diameter beyond the nanometer range.

If a method could fully utilize the contribution of conductive fillers, the percolation threshold could be decreased to minimize the strengthening effect of filler. Lately, there have been many studies focusing on lowering the percolation threshold by aligning the fillers in CPCs. Kim et al [35] presented a wearable pressure sensor made of a vertically aligned CNT prepared by CVD embedded into the PDMS matrix. Zhu et al [36] demonstrated combined top-down photolithography and bottom-up self-assembly growth strategy to fabricate oriented Au nanowires on PDMS for pressure sensing. However, these methods to align the conductive fillers including photolithography and CVD usually require an expensive and complicated process.

Herein, we report a conductive composite using PDMS as flexible matrix and magnetic μNi wires as conductive fillers. The diameter of μNi wire synthesized by liquid phase reduction method is around 1 μm with large aspect ratio of 150. When the composites are cured, the μNi wires can be aligned directly under external magnetic field in the thickness direction (Z-axis). This structure results in good electrical conductivity through the thickness of the film and the percolation threshold could decrease dramatically. The sensor with microhump microstructures molded by sandpaper exhibits ultrahigh sensitivity, wide sensing range and fast response time, which also shows potential for the application in clinical diagnosis.

2. Experimental section

2.1 Material

Nickel nitrate hexahydrate ($Ni(NO_3)_2·6H_2O$), hydrazine hydrate ($N_2H_4·H_2O$), ammonia ($NH_3·H_2O$) and sodium borohydride ($NaBH_4$) was provided by the Sinopharm Chemical Reagent Co., Ltd. Trichloro (1H, 1H, 2H, 2H-perfluorooctyl) silane was obtained from Sigma Aldrich. Sylgard 184 silicone elastomer was purchased from Dow Corning Corporation. All the chemicals were used as received without any further purification.

2.2 Synthesis of micro-nickel wires

$Ni(NO_3)_2·6H_2O$ (0.01 mol) was dissolved in ethanol (100 mL) with magnetic stirring for 20 min to get a clear green solution. $NaBH_4$ (0.13 mmol) was dissolved in $NH_3·H_2O$ (5 mL) to prevent the hydrolysis of $NaBH_4$ as $NaBH_4$ decomposes rapidly under acidic conditions. NaOH (0.02 mol) and $N_2H_4·H_2O$ (13 mL) were dissolved in deionized water (6.5 mL) as the reducibility of $N_2H_4·H_2O$ could be significantly enhanced with increasing of pH. Then, the $NaBH_4$ solution and the $N_2H_4·H_2O$ solution were both transferred into the as-prepared nickel nitrate solution in order at 60 °C under a magnetic field under stirring conditions. After 8 hours of reaction at 60 °C, a black substance was obtained floating on the surface of the solution. The resulting precipitates were washed three times with deionized water and ethanol respectively and then collected by placing a magnet under the beaker. The precipitates were dried in a vacuum oven at 60 °C for 12 h for further usage.

2.3 Fabrication of Ni@PDMS composites

The silicone elastomer base and curing agent were mixed at a ratio of 10:1. The μNi wires were dispersed at the desired volume fraction using a SpeedMixer (Flacktek) at 3000 rpm for 3 min to obtain a homogeneous mixture. The mixture was poured on the ITO glass deposited by Trichloro (1H, 1H, 2H, 2H-perfluorooctyl) silane and spin-coated at 500 rpm for 30 s to obtain Ni@PDMS film. Then, the film was placed in a vacuum oven for 10 min to remove bubbles. Two different processes were utilized to fabricate samples with random distribution of μNi wires (random sample) and alignment of μNi wires (aligned sample), respectively. For preparing the aligned sample, a pair of magnets were placed in the Z-axis direction of the composite, and the film was cured in a vacuum oven at 120 °C for 2 h under an external magnetic field (0.017 T). The random samples were obtained by directly curing the film in a vacuum oven at 120 °C for 2 h without applying magnetic field.

2.4 Characterization

The X-ray diffraction (XRD, Shimadzu7000) patterns were recorded to characterize μNi wires and Ni@PDMS composites using Cu Kα radiation（λ=1.5406 Å). The morphologies of μNi wires and Ni@PDMS composites were analyzed with a scanning electron microscope (SEM, Hitachi S4800) with an energy X-ray spectroscopic (EDS). A transmission electron microscope (TEM, JEOL 2100F) was performed to investigate the microstructure of μNi wires. Fourier transform infrared (FTIR) spectrum was recorded in the 500-2000 cm^{-1} under the total reflection mode by the FTIR spectrometer (Nicolet 5700). The distribution of μNi wires in PDMS was characterized by using a microcomputed tomography (Micro-CT) scanner (Nikon, XTH-225/320 LC). The electrical properties were tested by a LabVIEW controlled source meter (Keithley 2602A). The compression-pressure behaviors were acquired using a universal tensile testing machine (Shenzhen Suns Technology Stock Co. Ltd.) at a speed of 5 mm • min^{-1}.

3. Results and discussion

3.1 Characterization of μNi wires and Ni@PDMS composites

Fig. 1(a) shows the schematic illustration for the fabrication steps of Ni@PDMS composites and the μNi wires prepared by the liquid reduction method were mixed with PDMS by a SpeedMixer. Then the mixture was spin-coated on the top of ITO glass. Finally, it is cured in a magnetic field, and the μNi wires will be arranged along the direction of the magnetic field to achieve electrical conduction in the vertical thickness direction. The composites are highly flexible, stretchable and compressible subjected to various mechanical forces such as stretching, bending, twisting and even folding as illustrated in Fig. 1(b), indicating their great potential in serving as flexible piezoresistive sensor. As it can clearly be seen in Fig. 1(c), the aligned sample in the photograph exhibits better transparency than the random sample with the same content of μNi wires and the texts and pattern of Zhejiang University logo could be clearly observed. The size of the as-prepared Ni@PDMS composite is about 2 cm × 2 cm with a thickness of about 200 μm displayed in Fig. 1(d).

The μNi wires were prepared based on the liquid reduction method, in which $Ni(NO_3)_2 \cdot 6H_2O$ served as the nickel precursor, $N_2H_4 \cdot H_2O$ and $NaBH_4$ were used as reducing agents. The redox electromotive potential of $NaBH_4$ (-1.24 V) on Ni^{2+} is more negative than that of $N_2H_4 \cdot H_2O$ (-1.15 V) [], as shown in the reactions Eq. (1) and (2). Therefore, the reducibility of $NaBH_4$ to Ni^{2+} is greater than that of $N_2H_4 \cdot H_2O$. The synthesis mechanism of μNi wires can be divided into two parts: crystal nucleation and crystal grain growth. Firstly, many crystal nuclei were formed under the strong reducibility of Ni^{2+} by $NaBH_4$. Then, a larger number of Ni^{2+} were reduced further by adding $N_2H_4 \cdot H_2O$ and then coated on the previously formed crystal nuclei to grow into Ni particles. At last, the Ni particles were arranged in a line under the action of magnetic field, thereby forming a micron Ni wire structure.

$$N_2H_4 + 2Ni(OH)_2 = N_2 \uparrow + 2Ni + 4H_2O \quad \phi_1 = -1.15V \qquad \text{Eq. (1)}$$

$$2Ni^{2+} + 4BH_4^- + 9H_2O = Ni_2B \downarrow + 12.5H_2 \uparrow + 3B(OH)_3 \quad \phi_2 = -1.24V \qquad \text{Eq. (2)}$$

Fig. 2(a) is the SEM image of μNi wires and Fig. 2(b) is the corresponding image of higher magnification. According to the SEM images, the μNi wires are composed of many spherical particles chained one after another. The average diameter of μNi wires is around 1 μm and can be as long as 150 μm in length as shown in Fig. 2(c). These μNi wires are arranged in nearly parallel and are not entangled with each other. As can be seen in Fig. 2(d), the TEM image gives more information about the surface and interior structure of the μNi wire. Spiked nanoscale surface features can be observed on the surface of μNi wires. The high-resolution TEM (HRTEM) image in Fig. 2(e) displays the interplanar spacing of lattice fringe is 0.20 nm, which corresponds to the (111) plane of face-centered cubic (FCC) Ni. The selected area electron diffraction (SAED) patterns of μNi wires are shown in Fig. 2(f), confirming the successful synthesis of crystalline nickel.

The XRD results are shown in Fig. 2(g) and 2(h), which display the patterns of μNi wires, PDMS and Ni@PDMS composites with different volume fractions of μNi wires (2.49 vol%, 4.86 vol%, and 9.26 vol%). Compared with the standard XRD pattern of pure Ni, there are three characteristic diffraction peaks at $2\theta=44.5°$, 51.8°, and 73.4°, respectively corresponding to the (111), (200), and (220) crystal planes of FCC Ni [JCPDS Card No.04-0850] and the location of the peaks are shifted to lower angle with the volume fraction of Ni going up. The XRD patterns also show an amorphous peak at around 2θ value of 12° [37], which is in good agreement with the reported results [33] and the peak intensity decreases with the increase of volume fraction of Ni. It could be concluded that there are two phases in the composite: Ni and PDMS. The chemical structure of Ni@PDMS composites is characterized using an FTIR spectrometer as shown in Fig. 2(i). The FTIR spectra show characteristic peaks at approximately 786 cm^{-1}, 1008 cm^{-1}, and 1257 cm^{-1}, which are respectively attributed to $Si–(CH_3)_2$, Si-O-Si and $Si-CH_3$, which provide evidence for the formation of PDMS. Therefore, all the results show the successful preparation of μNi wires and PDMS, confirming the incorporation of μNi wires into PDMS.

3.2 Morphology of μNi wires in PDMS under external magnetic field

The prepared μNi wires with aspect ratio of 150 were combined with PDMS matrix to obtain a series of composites with different volume fractions of conductive fillers. During the curing process of the composites, an external magnetic field is applied along the thickness of the composites (Z-axis). The Micro-CT images show that the μNi wires are turned and finally aligned with the outer magnetic field under the action of the external magnetic field as shown in Fig. 3(a). In the top view, only the outcrops but no main body of μNi wires are evenly distributed in PDMS. In the side view, it can be observed that the μNi wires are arranged in parallel along with the thickness direction. In the three-dimensional diagram, the μNi wires can be observed to evenly disperse in the matrix. The cross-sectional SEM images can also verify the alignment of μNi wires in the magnetic direction, as shown in Fig. 3(c), which shows images of 0.26 vol% aligned Ni@PDMS sample and μNi wire are observed to be vertical to the surface of the film. Therefore, it can be concluded that the μNi wires are uniformly distributed in the PDMS matrix and oriented in the thickness direction. In contrast, the outcrops of the μNi wires are distributed on the cross section of composites of 3.69 vol% random Ni@PDMS sample shown in Fig. 3(d), which indicates that the direction of μNi wires in the matrix is random.

In a ferromagnetic system, the total free energy (E_{total}) is the summation of five magnetic energy components, which are external magnetic field energy (E_{field}), demagnetization field energy (E_d), magnetic exchange energy (E_{ex}), magnetoelastic energy (E_{el}) and magnetocrystalline anisotropy energy (E_σ) [38]. Here, only E_{field} and E_d are needed to be considered, which are caused by the interaction between surface magnetic poles and the shape anisotropy of μNi wires. E_{field} is determined by the magnetic field and magnetization, as shown in Eq. (3). The ferromagnet has energy in the magnetic field and also has a certain potential energy in the demagnetizing field generated by itself, namely demagnetizing field energy. The E_d can be calculated by Eq. (4).

$$E_{field} = \mu_0 MH \sin\theta \qquad \text{Eq. (3)}$$

$$E_d = -\int_0^M \mu_0 H_d dM = \frac{1}{2}\mu_0 NM^2 \qquad \text{Eq. (4)}$$

where μ_0 is vacuum permeability, M is the magnetization, H is the magnetic field, θ is the angle between M and H, and N is the demagnetization factor which is only related to the shape of the material. As shown in Fig. 3(b), when there is no external magnetic field, the magnetic domains inside the μNi wire are in disorder, and the macroscopic magnetization is close to zero. When the angle between the direction of the external magnetic field and the μNi wire is θ, magnetic field could be resolved into an axial magnetic field ($H_{//}$) and a transversal one ($H_\perp$) and induce magnetic dipoles along two orthogonal directions. Thus, the direction of the two orthogonal demagnetization fields ($H_{d,\perp}$ and $H_{d,//}$) is opposite to the direction of external magnetic field while the direction of magnetization is from N pole to S pole. Since μNi wires have shape anisotropy, the greater the aspect ratio, the higher the anisotropy, and the shape factor along the long axis direction will be close to zero, so the demagnetization field can be minimized when magnetized along the long axis direction according to Eq. (4). Due to the interaction between the magnetic dipole moment and the external magnetic field according to Eq. (3), the angle between *M* and *H* will be close to zero. Therefore, the μNi wire will turn to the direction consistent with the magnetic field under the action of the torque, so as to reach the state with the lowest static magnetic energy. As a result, this could explain why μNi wires would turn to the direction along the external magnetic field when the composites are cured.

3.3 Electrical characterization of Ni@PDMS composites

The electrical conductivity through the thickness of the composites was tested by a LabVIEW controlled source meter and a voltage of 1 V was applied between the top and bottom electrodes. As shown in Fig. 4(a) and 4(b), the electrical conductivity of composites for random samples and aligned samples both goes up with the volume fraction of the conductive filler increasing. When the volume fraction reaches the percolation threshold, a conductive network will form throughout the system, so the conductivity will increase rapidly near the percolation threshold and the law obeys the following Eq. (5) [32]:

$$\sigma = \sigma_0(\varphi - \varphi_c)^t \qquad \text{Eq. (5)}$$

where the percolation threshold φ_c could be obtained by taking the logarithmic transformation on the left and right sides of the equation at the same time and perform liner fitting. The percolation threshold of the aligned samples is about 0.31 vol%, which is much lower than the percolation threshold (4.79 vol%) of the samples with random fillers. It indicates that the percolation threshold can greatly decrease by the directional arrangement of the conductive fillers. However, the percolation threshold of sample with random μNi wires is much smaller than that (5 vol%) with Ni nanowires [39] and with Ni particles (15 vol%) [40], which is similar to the results reported in CNT-PDMS system [41].

The two mechanisms contributing to the electrical conductivity of Ni@PDMS composites are conductive networks and electron tunneling. The resistance of the network contains the intrinsic resistance of μNi wires and the tunneling resistance. As shown in Fig. 4(c) and 4(d), they are the representative elements of random sample and aligned sample. The cuboid represents polymer matrix PDMS and the eight yellow line segments represent μNi wires. In order to describe the degree of orientation of μNi wires dispersed in PDMS, the angle θ between x_3 axis and μNi wire is introduced, where the x_3 axis is consistent with the direction of the external magnetic field. The electrical resistivity of the representative element in the vertical direction is described as Eq. (8).

$$\rho = \frac{(R_{tunnel} + R_c)L_{Ni}\sin^2\theta}{\cos\theta} \qquad \text{Eq. (8)}$$

where L_{Ni} is the length of μNi wire and θ represents the angle between μNi wire and the vertical direction, $\sin\theta = \sqrt{3}/3$ represents the random sample (Fig. 4(c)). Also, the values of intrinsic resistance R_i and tunnel resistance R_{tunnel} remain unchanged assuming that only the direction of the conductive phase changes. It can be found that as the angle decreases (Fig. 4(d)), the resistivity decreases, which also means that the higher the degree of orientation, the higher the electrical conductivity. This could explain the significant decrease of percolation threshold in the orientation system compared with the random system.

3.4 Piezoresistive performance of Ni@PDMS composites

The percolation effect means that as the volume fraction of the conductive filler increases, the composites could achieve a transition from the insulator to conductor. When the volume fraction of the conductive filler does not reach the percolation threshold, the sample also has a piezoresistive effect, which means that the resistance of composites decreases as the applied pressure increases. This threshold pressure is determined to be the lowest pressure at which the sample shows conductivity $>10^{-9}$ S/m. In order to better understand the change of electrical conductivity of the Ni@PDMS composites under varying pressure loading, samples were fabricated with different volume fractions but the same magnetic field (17 mT). As shown in Fig. 5(a), the electrical conductivity versus pressure response of the samples is measured to obtain the threshold pressure of Ni@PDMS with the loading rate of 5 mm • min^{-1}. The measured conductivity of the composite film containing 0.025 vol% fillers is maintained at almost 10^{-9} S/m during the compression. At this low content, the composite is not piezoresistive within the range of applied pressure (<150 kPa). In samples with higher volume fractions, the conductivity of the samples is around 10^{-9} S/m before the threshold pressure, which is close to the conductivity of the PDMS matrix. When the pressure is close to the threshold pressure, the conductivity will change several orders of magnitude. And as the content of the conductive filler increases, the threshold pressure decreases. The volume fraction of the filler is 0.05 vol%, 0.30 vol% and 0.60 vol% the corresponding threshold pressure is 66 kPa, 15 kPa, 1 kPa. When the volume fraction of the filler reaches 1.20 vol%, the conductivity of the sample directly reaches 0.8 S/m at zero pressure, indicating that a complete percolation network is formed in the sample. However, for samples with randomly distributed μNi wires, the measured electrical conductivity of the composite film containing 3.69 vol% fillers maintained at almost 10^{-9} S/m during the compression as shown in Fig. 5(b). The volume fraction of the filler is 5.10 vol %, 6.00 vol% and 7.10 vol% and the corresponding threshold pressure is 88 kPa, 45 kPa and 0.3 kPa.

To understand the mechanism of how the content of fillers influences the threshold pressure for low-to-high conductivity transition, a simplified model is proposed as schemed in Fig. 5(c) and Fig. 5(d). When pressure is applied on the film along the thickness direction, the μNi wires will approach each other so that the probability of tunneling increases and thus the conductivity will increase. As the pressure increases, the μNi wires could also form many conductive paths in the thickness direction, the corresponding pressure is the threshold pressure. The percolation pressure decreases with increasing volume fraction, which indicates that the sensing range of piezoresistive sensors based on Ni@PDMS composites can be adjusted by the fraction of conductive filler. There exist two kinds of non-contact modes in random and aligned samples: one is the overlapping non-contact and the other is the head-to-tail non-contact. As shown in Fig. 5(c) and 5(d), when the volume fraction of μNi wire is the same in these two conditions, more electrons could tunnel in the head-to-tail non-contact mode than the overlapping non-contact mode under the same applied pressure. In other words, more conductive paths could come into being in the oriented sample as shown in Fig. 5(c1) and 5(d1), the red line indicates the passage of current. Therefore, it requires greater pressure to achieve the formation of conductive network under the same amount of conductive filler for random samples.

3.5 Performance of the pressure sensor based on Ni@PDMS composites with microhump structure

The sensitivity and work range are the crucial parameters of the piezoresistive sensor. In order to obtain both high sensitivity and wide sensing range, the Ni@PDMS composite with a volume fraction of 0.60 vol % was selected for the preparation of the single sensing layer of the piezoresistive sensor. The sensor consists of a sensing layer with microhump structure between top and bottom electrodes (Fig. 6(a)). Fig. 6(b) shows the SEM image of microhump structures of Ni@PDMS composite and sandpapers were used as molding templates to develop the microhump microstructures to increase the sensitivity further. The test system including a digital force gauge for applying pressure, a Keithley digital source meter for detecting electrical signal and a computer for collecting data. The force gauge applied the pressure on the sensor and the digital source meter measures the current driven by a voltage of 1V at the same time. Sensitivity is defined as follows:

$$S = \frac{\Delta I / I_0}{\Delta P} \qquad \text{Eq. (9)}$$

where I_0 is the initial current without pressure, ΔI is the variation of current under external pressure and ΔP is the variation of pressure. Fig. 6(c) depicts the plots of $\Delta I / I_0$ versus ΔP of the piezoresistive sensor based on aligned Ni@PDMS composite without microstructure and with microhump structure. For the sensor with microhump structure, the sensitivity is 8706 kPa^{-1} in the low-pressure regime (1 kPa-24 kPa) and the sensitivity is 699 kPa^{-1} in the high-pressure regime (24 kPa-120 kPa). The sensitivity of device without microstructure is 4327 kPa^{-1} in the low-pressure regime and is 232 kPa^{-1} in the high-pressure regime (Fig. 6(c) and 6(d)). It is big variation of the current derived from the tunneling effect under exerted pressure that the piezoresistive sensor based on aligned Ni@PDMS achieves an ultra-high sensitivity. Furthermore, it can be concluded that microhump structure will make contributions to the higher sensitivity due to the change of contact area of electrodes and composites. Moreover, the Ni@PDMS composites with a volume fraction near the percolation threshold have high conductivity, in the meanwhile the volume fraction is slightly larger than the percolation threshold which can ensure a lower percolation pressure to obtain a broad response range. Fig. 6(e) displays the current-time curves of the sensor under the varying pressure (5kPa, 7kPa, 9kPa, 24kPa, 50kPa, 100kPa) for about 1 min. The current remains almost stable under a fixed pressure for a minute, which proves excellent stability of the device. Fig. 6(f) demonstrates that the response time and relaxation time of the sensor under 5 kPa are 25 ms and 20 ms, respectively. The fast response time ensures a timely response under external pressure, which is essential in practical applications. Fig. 6(g) represents the current-voltage curves of the sensor under different pressure with the voltage ranging from -0.5 V to 0.5 V and the linear relationship between voltage and current indicates the Ohmic contact between electrodes and the composites and the stable network in composites. Besides, the increase in slope with increasing pressure is due to the increase in conductance caused by the increase of conductive paths. Also, the current typically increases as the pressure increases thus the device could distinguish the different pressure and has extraordinary repeatability. The weight with 20 g, 50 g and 100 g can result in distinct current as shown in Fig. 6(h), which exhibits the device has superior ability to dynamically detect the whole range of blood pressure ranges from 4.7 kPa for infants to 21 kPa for hypertensive patients. Fig. 6(i) exhibits the comparison between the lasted reported literature and our work. As far as we know, the piezoresistive sensor that can both enable such high sensitivity (9081kPa^{-1}) and wide detection range (~120 kPa) are scarcely reported.

3.6 In vitro sensor characterization

CABG remains the standard surgery for patients with CHD and verifying whether a narrowing or blocking occurs or not is a key to assure the success of the surgery. As shown in Fig. 7(a), the problem of judging the patency of blood vessels after bridging can be simplified to confirm whether there is narrowing or block after the blood vessel is sutured. The sensor was characterized in vitro in a pump-driven system that mimics the pulsatile behavior and typical expansion of the coronary artery. As shown in Figure 7b, a PVA tube is used to simulate an artificial blood vessel and one end is connected to a water pump that can drive pulsed water waves. The polyethylene film is utilized to package the piezoresistive senor to achieve electrical signal stability in the underwater environment. Then the device was wrapped around the PVA tube with a diameter of 7 mm which is about the same size as the people's coronary artery. After the water flows out of the pump, it passes through the PVA tube and then flows back to the pump. It is like that blood starts from the heart, flowing through arteries and veins, and returns to the heart. When a pulse passes through the PVA tube, the tube could expand and contract, hence the sensor in close contact with tube can detect the deformation and convert the deformation into electrical signal shown in Fig. 7(c) and Fig. 7(d). The coronary artery frequency of normal adults is 1 Hz~2 Hz, so the test frequency is set at 0.8 Hz, 1.6 Hz and 2.4 Hz. Figure 7(e) shows the various current response of the sensor under different amplitudes at the frequency of 1.6 Hz, that is, the response under different flow rate conditions. When the flow rate increases, the current signal increases in response, indicating that the sensor could stably monitor the pressure signal generated by the blood flow under low flow rate conditions. Fig. 7(f) illustrates the current response at different vibration frequencies. The frequencies of the sensor current waveforms are 0.8 Hz, 1.6 Hz and 3.2 Hz. This demonstrates that the vibration frequency and flow rates of different fluids can be detected by the response of the current, revealing the huge potential application of the device in monitoring the blood flow of the human body.

4. Conclusion

Ni@PDMS composites are fabricated as single sensitive layer for flexible piezoresistive pressure sensors by introducing electrically conductive μNi wires evenly into PDMS matrix. Benefiting from the adjustable conductive network, the Ni@PDMS exhibited tunable piezoresistive effect according to the volume fraction of μNi wires. The designed conductive composite with aligned μNi wires exhibits a lower percolation threshold comparing to random arrangement. As a result, the sensor based on 0.60 vol% aligned Ni@PDMS composite exhibited high sensitivity (8706 kPa^{-1}), a wide sensing range (~120 kPa) and fast response time (~22 ms). Finally, the flexible sensors are demonstrated to monitor different frequencies and flow rates of water flow in vitro in a pump-driven system that mimics the pulsatile behavior and typical expansion, showing potential application in monitoring vessel patency which is critical to patient recovery.

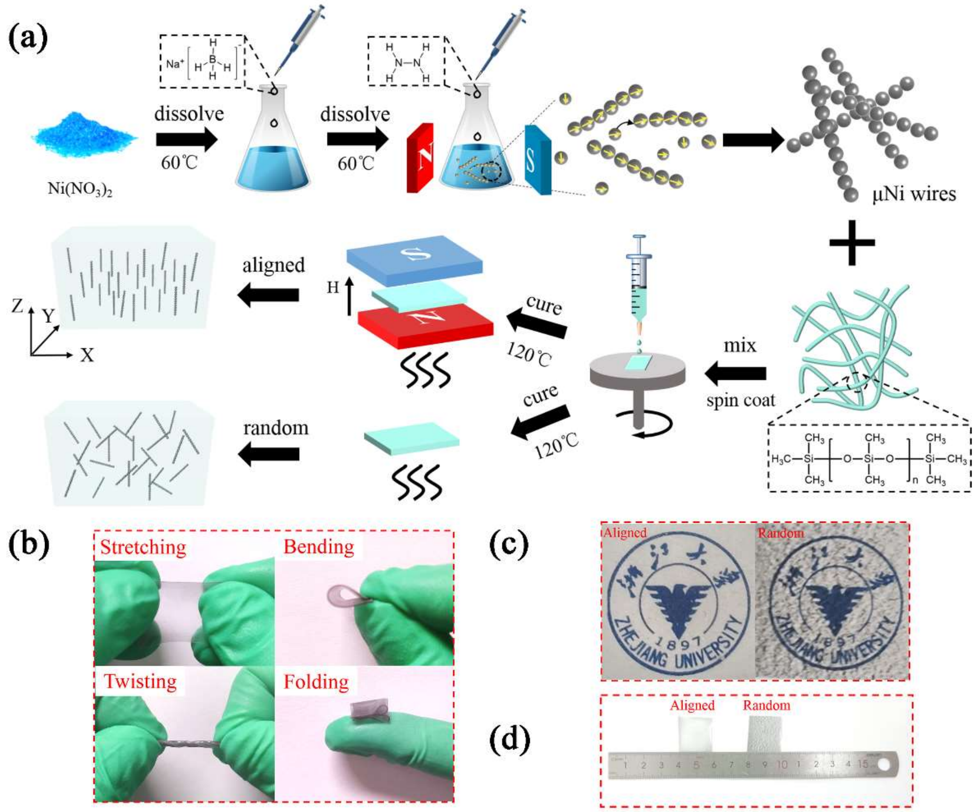

Fig. 1. (a) Schematic diagram of the process of the preparation of the μNi wires and the composite film. (b) Photograph of Ni@PDMS composites under various mechanical forces. (c) Comparison of transparency of aligned sample and random sample at the same filler content. (d) The top optical image of aligned sample and random sample.

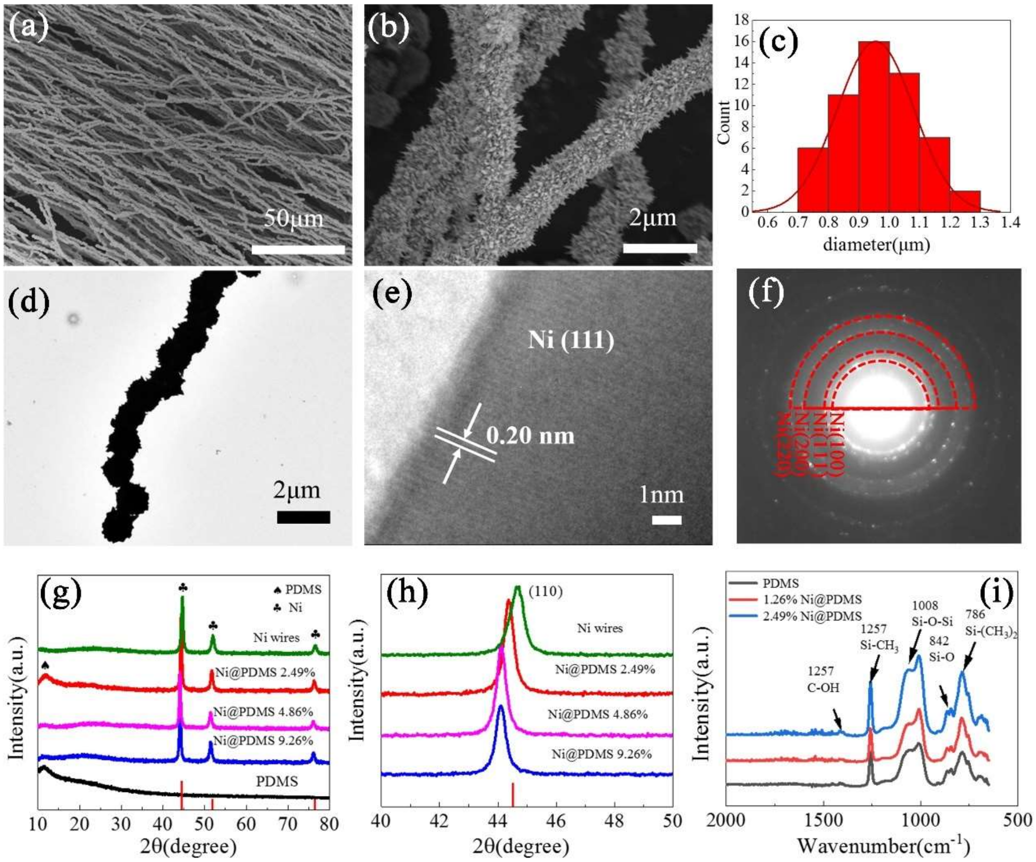

Fig. 2. (a) Low-magnification SEM image of μNi wires. (b) Enlarged SEM image of μNi wires. (c) Diameter distribution graph of μNi wires. (d) TEM image of an individual μNi wire. (e) HRTEM image of μNi wires. (f) SAED pattern of μNi wire with the scale bar of 1/5 nm. (g) (h) XRD patterns of Ni@PDMS composites (random) with different volume fractions (2.49 vol%, 4.86 vol% and 9.26 vol%, respectively), μNi wires and PDMS. (i) FTIR spectrum of Ni@PDMS composites (random) with different volume fractions (1.26 vol% and 2.49 vol%) and PDMS.

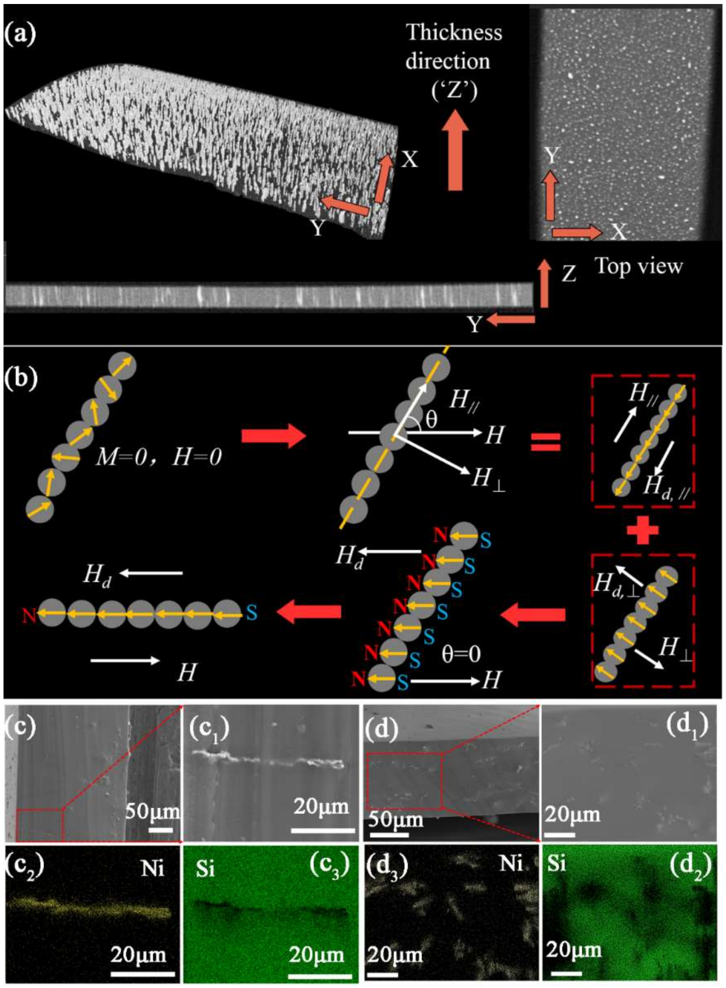

Fig. 3. (a) Micro-CT images of aligned 0.15 vol% Ni@PDMS composite. (b) Mechanism diagram of the alignment of μNi wires in PDMS during curing process under an external magnetic field. (c) SEM images and elemental mappings of the section of 0.26 vol% Ni@PDMS composite (aligned). (d) SEM images and elemental mappings of the section of 3.69 vol% Ni@PDMS composite (random).

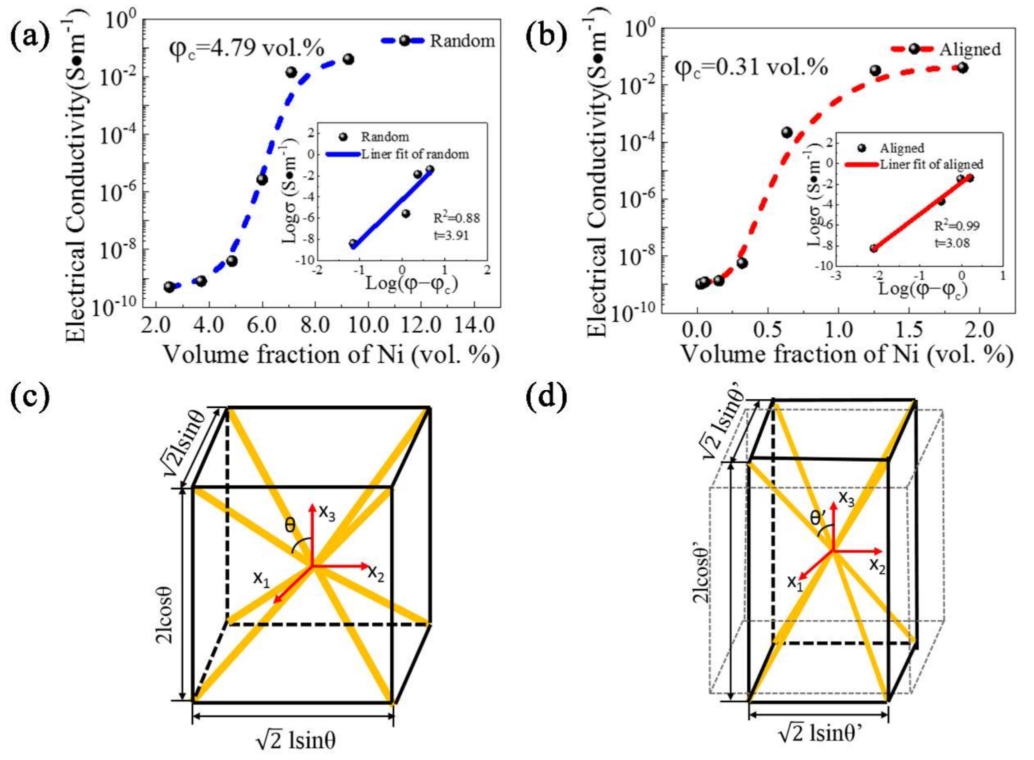

Fig. 4. The electrical conductivity of Ni@PDMS composites (a) random (b) aligned versus volume fraction of Ni. The inset is line of log σ versus log $(\varphi - \varphi_c)$. Schematic illustration of the eight-chain model (c) random and (d) aligned. The yellow line represents the μNi wire, and l is the length of the μNi wire.

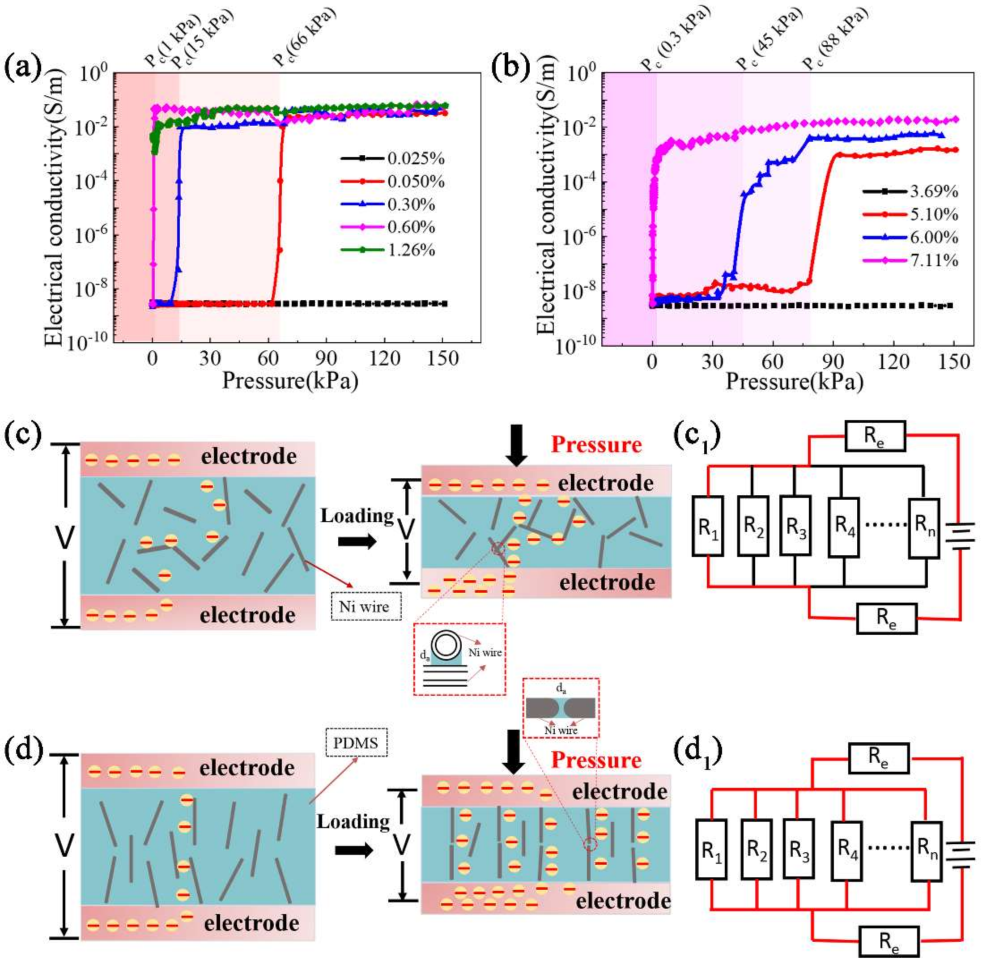

Fig. 5. Piezoresisvity of Ni@PDMS composites (a) random (b) aligned with different filler fraction and the corresponding percolation pressure to different volume fraction. Schematic diagram of Ni@PDMS composite of conductive mechanism of (c) random (d) aligned.

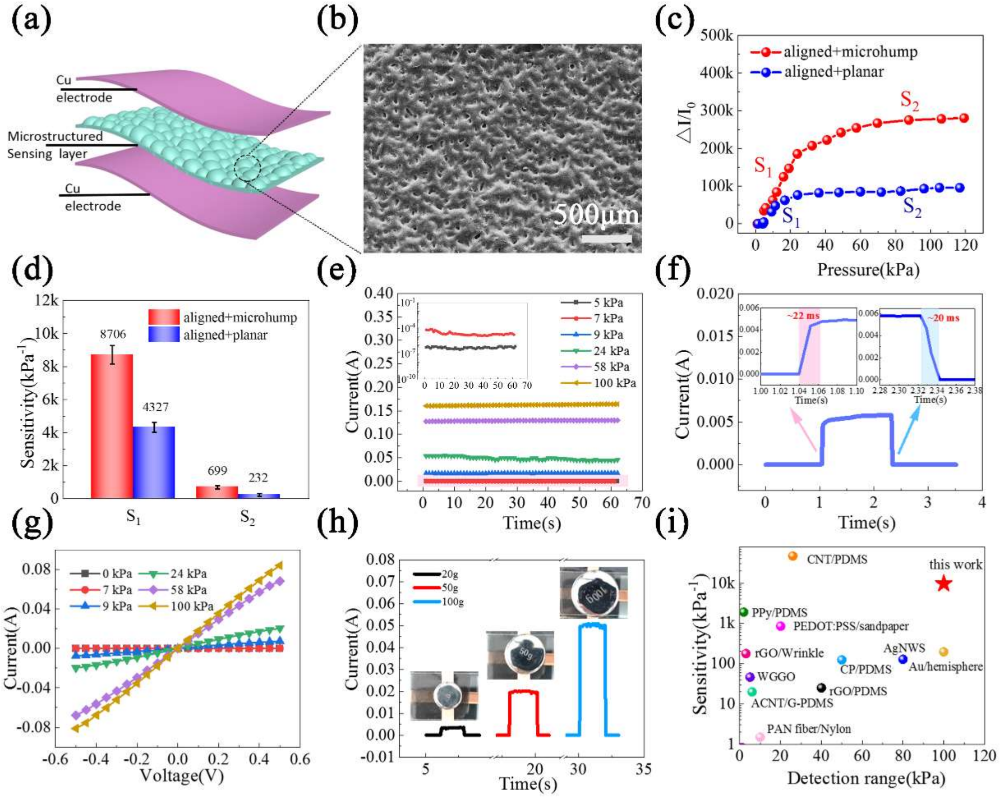

Fig. 6. (a) Schematic of the structure of piezoresistive pressure sensor. (b) SEM image of microstructured Ni@PDMS composite film. (c) The $\Delta I/I_0$ versus pressure curve of piezoresistive sensor based on the 0.6 vol% aligned Ni@PDMS composite. (d) Sensitivity of piezoresistive sensor with hierarchical structure and without structure. (e) I-T curves of the sensor under a series of pressure for 1 min. (f) Response time and recovery time of the sensor. (g) I-V curves of the sensor from -0.5 V to 0.5 V. (h) Different current response of sensor to 20 g, 50 g and 100 g weights. (i) The performance comparison of this work to the state-of-art literature.

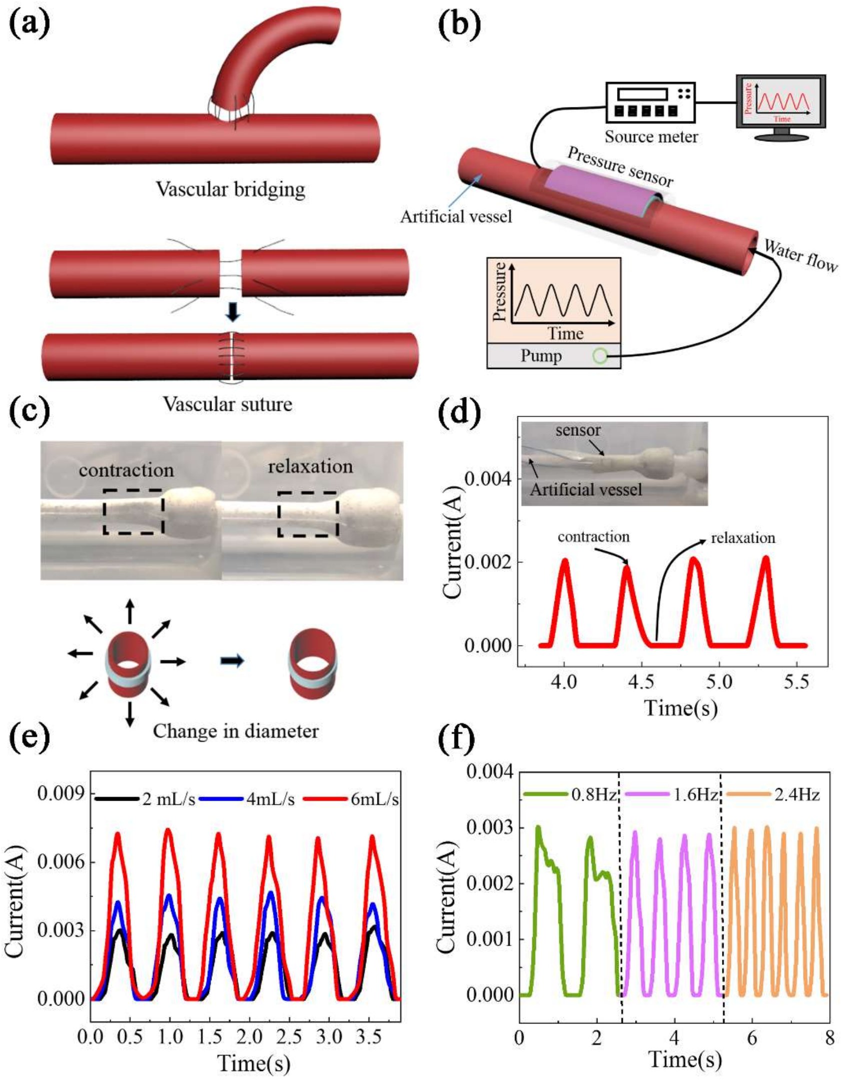

Fig. 7. (a) Schematic diagram of vascular bridging and vascular suture. (b) Demonstration of the piezoresistive pressure on the pump-driven water system simulating the blood flow in blood vessels. (c) Expansion and contraction of tube and (d) the corresponding current response. (e) Current responses at various vibration amplitudes with a frequency of 1.6 Hz. (f) Current responses at different vibration frequencies with the flow rate of 2 mL/s.

TOC

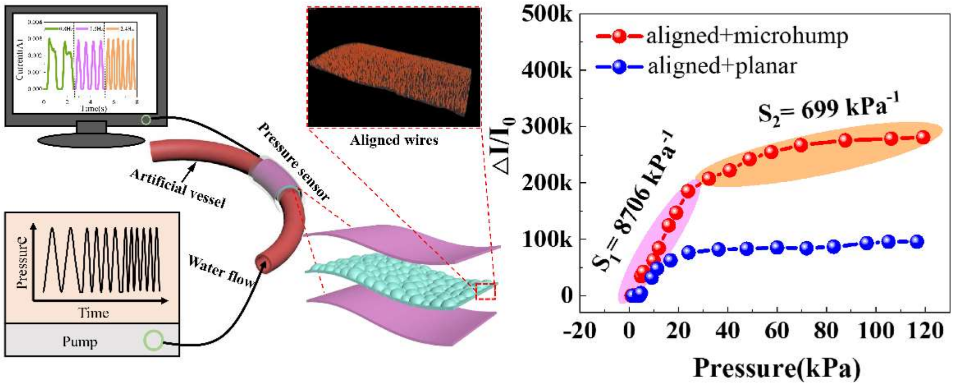

Declaration of Competing Interest

There are no conflicts of interest to declare.

Acknowledgements

This work was supported by the National Natural Science Foundation of China (Grant Numbers 51702285, 91748209. The authors also want to acknowledge the support of funding of Key Research and Development Program of Zhejiang Province (2020C05010), and the Fundamental Research Funds for the Central Universities (No. 2020XZZX005-02).

References

1. C. L. Choong, M. B. Shim, B. S. Lee, S. Jeon, D. S. Ko, T. H. Kang, J. Bae, S. H. Lee, K. E. Byun, J. Im, Y. J. Jeong, C. E. Park, J. J. Park and U. I. Chung, *Adv. Mater.*, 2014, **26**, 3451-3458.
2. S. Gong, W. Schwalb, Y. Wang, Y. Chen, Y. Tang, J. Si, B. Shirinzadeh and W. Cheng, *Nat. Commun.*, 2014, **5**, 3132.
3. L. Wang, H. Wang, X.-W. Huang, X. Song, M. Hu, L. Tang, H. Xue and J. Gao, *J. Mater. Chem. A*, 2018, **6**, 24523-24533.
4. T. Yamada, Y. Hayamizu, Y. Yamamoto, Y. Yomogida, A. Izadi-Najafabadi, D. N. Futaba and K. Hata, *Nat. Nanotechnol.*, 2011, **6**, 296-301.
5. Q. Zhou, B. Ji, Y. Wei, B. Hu, Y. Gao, Q. Xu, J. Zhou and B. Zhou, *Adv. Funct. Mater.*, 2019, **7**, 27334-27346.
6. E. Cetin, M. Tola, Z. Iscan, A. Ozyuksel and K. Cagli, *Journal-Cardiovascular Surgery*, 2014, **2**, 1-5.
7. C. Stefanadis, C.-K. Antoniou, D. Tsiachris and P. Pietri, *J Am Heart Assoc*,

2017, **6**, 1-18.

8. P. W. Serruys, M.-C. Morice, A. P. Kappetein, A. Colombo, D. R. Holmes, M. J. Mack, E. Ståhle, T. E. Feldman, M. v. d. Brand, E. J. Bass, N. V. Dyck, K. Leadley, K. D. Dawkins and F. W. Mohr, *The new england journal of medicine*, 2009, **360**, 961.
9. Y. Nakahara, S. Yoshida, Y. Yamamoto, H. Uemura, S. Yamagishi, K. Furuhata, Y. Hanzawa, T. Kanemura and S. Osaka, *Gen Thorac Cardiovasc Surg*, 2017, **65**, 285-288.
10. B. F. Buxton, P. A. R. Hayward, A. E. Newcomb, S. Moten, S. Seevanayagam and I. Gordon, *Eur J Cardiothorac Surg*, 2009, **35**, 658-670.
11. M. Leacche, J. M. Balaguer and J. G. Byrne, *Semin Thorac Cardiovasc Surg*, 2009, **21**, 207-212.
12. P. Lehnert, C. H. Moller, S. Damgaard, T. A. Gerds and D. A. Steinbruchel, *J Card Surg*, 2015, **30**, 47-52.
13. J. J. Jokinen, K. Werkkala, T. Vainikka, T. Perakyla, J. Simpanen and L. Ihlberg, *Eur J Cardiothorac Surg*, 2011, **39**, 918-923.
14. D. X. Zhao, M. Leacche, J. M. Balaguer, K. D. Boudoulas, J. A. Damp, J. P. Greelish and J. G. Byrne, *J Am Coll Cardiol*, 2009, **53**, 232-241.
15. C. M. Boutry, L. Beker, Y. Kaizawa, C. Vassos, H. Tran, A. C. Hinckley, R. Pfattner, S. Niu, J. Li, J. Claverie, Z. Wang, J. Chang, P. M. Fox and Z. Bao, *Nat Biomed Eng*, 2019, **3**, 47-57.
16. B. C.-K. Tee, C. Wang, R. Allen and Z. Bao, *Nat Nanotechnol*, 2012, **7**, 825-832.
17. M. Amit, L. Chukoskie, A. J. Skalsky, H. Garudadri and T. N. Ng, *Adv. Funct. Mater.*, 2019, DOI: 10.1002/adfm.201905241, 1905241.
18. L. Li, J. Zheng, J. Chen, Z. Luo, Y. Su, W. Tang, X. Gao, Y. Li, C. Cao, Q. Liu, X. Kang, L. Wang and H. Li, *Adv. Mater. Interfaces*, 2020, **7**, 2000743.
19. Y. Zang, F. Zhang, C.-a. Di and D. Zhu, *Materials Horizons*, 2015, **2**, 140-156.
20. B. Su, S. Gong, Z. Ma, L. W. Yap and W. Cheng, *Small*, 2015, **11**, 1886-1891.
21. C. M. Boutry, A. Nguyen, Q. O. Lawal, A. Chortos, S. Rondeau-Gagne and Z. Bao, *Adv Mater*, 2015, **27**, 6954-6961.
22. Z. Wang, S. Wang, J. Zeng, X. Ren, A. J. Y. Chee, B. Y. S. Yiu, W. C. Chung, Y. Yang, A. C. H. Yu, R. C. Roberts, A. C. O. Tsang, K. Wing and P. K. L. Chan, *Small*, 2016, **12**, 3827-3836.
23. S. Wang, G. Chen, S. Niu, K. Chen, T. Gan, Z. Wang, H. Wang, P. Du, C. Leung and S. Qu, *ACS applied materials & interfaces*, 2019, **11**, 48331-48340.
24. H. Yao, J. Ge, C. Wang, X. Wang, W. Hu, Z. Zheng, Y. Ni and S. Yu, *Adv. Mater.*, 2013, **25**, 6692-6698.
25. Y. Song, H. Chen, Z. Su, X. Chen, L. Miao, J. Zhang, X. Cheng and H. Zhang, *Small*, 2017, **13**, 1702091.
26. Z. Wang, X. Guan, H. Huang, H. Wang, W. Lin and Z. Peng, *Adv. Funct. Mater.*, 2019, **29**, 1807569.
27. H. Weina, L. Guangyong, Z. Changsheng, Z. Shangquan, Y. Wei, W. Jin, L. Qingwen and Z. Xuetong, *ACS Nano*, 2015, 4244-4251.

28. Q. Sun, X. Zhao, Y. Zhou, C. Yeung, W. Wu, S. Venkatesh, Z. Xu, J. J. Wylie, W. Li and V. A. L. Roy, *Adv. Funct. Mater.*, 2019, **29**, 1808829.
29. X. Wu, Y. Han, X. Zhang, Z. Zhou and C. Lu, *Adv. Funct. Mater.*, 2016, **26**, 6246-6256.
30. Y. Jiang, Y. Wang, Y. K. Mishra, R. Adelung and Y. Yang, *Adv. Mater. Technologies*, 2018, **3**, 1800248.
31. I. Balbegr, D. Azulay, D. Toker and O. Millo, *International Journal of Modern Physics B*, 2004, **18**, 2091-2121.
32. S. Kirkpatrick, *Rev. Mod. Phys.*, 1973, **45**, 574-588.
33. H. Denver, T. Heiman, E. Martin, A. Gupta and D.-A. Borca-Tasciuc, *J. Appl. Phys.*, 2009, **106**.
34. S. Khan and L. Lorenzelli, *Smart Materials and Structures*, 2017, **26**.
35. K.-H. Kim, S. K. Hong, N.-S. Jang, S.-H. Ha, H. W. Lee and J.-M. Kim, *ACS applied materials & interfaces*, 2017, **9**, 17499-17507.
36. B. Zhu, Y. Ling, L. W. Yap, M. Yang, F. Lin, S. Gong, Y. Wang, T. An, Y. Zhao and W. Cheng, *ACS applied materials & interfaces*, 2019, **11**, 29014-29021.
37. D. Sun, B.-B. Li and Z.-L. Xu, *Korean Journal of Chemical Engineering*, 2013, **30**, 2059-2067.
38. C. Zhang, T. Ma and M. Yan, *J. Appl. Phys.*, 2011, **110**.
39. J.-M. Park, S.-J. Kim, D.-J. Yoon, G. Hansen and K. L. DeVries, *Composites Science and Technology*, 2007, **67**, 2121-2134.
40. S. H. Jang, Y. L. Park and H. Yin, *Materials (Basel)*, 2016, **9**.
41. J. Li, P. C. Ma, W. S. Chow, C. K. To, B. Z. Tang and J. K. Kim, *Adv. Funct. Mater.*, 2007, **17**, 3207-3215.